GEOPHYSICS, VOL. 73, NO. 4 (JULY-AUGUST 2008); P. D41–D51, 8 FIGS., 3 TABLES.
10.1190/1.2931680

The effect of microstructure and nonlinear stress on anisotropic seismic velocities

James P. Verdon[1], Doug A. Angus[1], J. Michael Kendall[1], and Stephen A. Hall[2]

ABSTRACT

Recent work in hydrocarbon reservoir monitoring has focused on developing coupled geomechanical/fluid-flow simulations to allow production-related geomechanical effects, such as compaction and subsidence, to be included in reservoir models. To predict realistic time-lapse seismic signatures, generation of appropriate elastic models from geomechanical output is required. These elastic models should include not only the fluid saturation effects of intrinsic, shape-induced, and stress-induced anisotropy, but also should incorporate nonlinear stress-dependent elasticity. To model nonlinear elasticity, we use a microstructural effective-medium approach in which elasticity is considered as a function of mineral stiffness and additional compliance is caused by the presence of low-aspect ratio displacement discontinuities. By jointly inverting observed ultrasonic P- and S-wave velocities to determine the distribution of such discontinuities, we assessed the appropriateness of modeling them as simple, planar, penny-shaped features. By using this approximation, we developed a simple analytical approach to predict how seismic velocities will vary with stress. We tested our approach by analyzing the elasticity of various sandstone samples; from a United Kingdom continental shelf (UKCS) reservoir, some of which display significant anisotropy, as well as two data sets taken from the literature.

INTRODUCTION

During the past 15 years, the use of temporal variations in seismic properties (4D or time-lapse seismic) has become an important tool in locating zones of unproduced hydrocarbons, improving drilling strategies, and increasing production. Specifically, time-lapse seismic has been used as a tool for identifying zones of fluid replacement (e.g., where hydrocarbons have been replaced by water during production). However, it is becoming increasingly clear that fluid substitution alone cannot account for all observed temporal variations of time-lapse seismic data (see, e.g., Hatchell and Bourne, 2005). For example, observation of large-scale subsidence at Ekofisk (e.g., Guilbot and Smith, 2002) and other highly compressible reservoirs, wellbore failures (e.g., McLellan, 1996), and fault reactivation have highlighted the importance of considering geomechanical effects in reservoir modeling.

Although well developed and routinely applied in tunneling and mining industries, the use of geomechanics in the hydrocarbon industry is relatively recent. An important development in the hydrocarbon industry is the coupling of fluid-flow effects within the reservoir with geomechanical deformation of the reservoir and surrounding nonpay units (e.g., Dean et al., 2003). Minkoff et al. (2004) apply coupled fluid-flow/geomechanical simulation to show how production can reduce pressure inside a reservoir, resulting in compaction, surface subsidence, and reduction of P-wave velocities. Along with modeling production-induced compaction, coupled fluid-flow/geomechanical simulators are beginning to be used to study other problems such as repressurization and inflation caused by CO_2 or steam injection, fault-reactivation/top-seal failure, and stress arching and extension in the overburden.

To relate geomechanical simulations to time-lapse seismic observations, we must have a method capable of adapting geomechanical output (e.g., in situ stresses and strains, changes in porosity, and the movement and properties of fluid within the reservoir) into a dynamic elastic model for seismic forward-modeling applications (e.g., ray tracing, full- and/or directional-wave solutions). Several methods are available to account for effects of fluid properties and changes in porosity on seismic properties. At low frequencies (e.g., that of most seismic waves), the Gassmann equations (Gassmann, 1951) are valid and are used widely, and this approach has been extended to include anisotropic rocks (Brown and Korringa, 1975). However, we also must account for changes in elasticity of reservoir and nonpay rocks caused by changes in the applied stress and strain.

Manuscript received by the Editor 26 November 2007; revised manuscript received 21 January 2008; published online 1 July 2008.
[1]University of Bristol, Department of Earth Sciences, Bristol, U. K. E-mail: gljpv@bris.ac.uk; D.Angus@bris.ac.uk; gljmk@bris.ac.uk.
[2]Institut de Mécanique de Grenoble, Grenoble, France. E-mail: hall@geo.hmg.inpg.fr.

Effects of stress and/or strain on rock elasticity are observed empirically to be nonlinear (e.g., Nur and Simmons, 1969). The stress dependence of seismic velocities is strong at low-confining stresses but weakens as confining stresses increase. The most common explanation for this observation is that at low pressures, seismic velocities are dominated by changes in number density of small cracks or discontinuities between grain boundaries. At higher pressures, these cracks close and velocities increase but become less dependent on stress. Many approaches have been used to account for this nonlinearity, including empirically determined relationships (Minkoff et al., 2004), Hertz-Mindlin contact forces (e.g., Makse et al., 1999), third-rank elasticity tensors (e.g., Prioul et al., 2004), and microstructural modeling.

Many microstructural models exist (e.g., Zatsepin and Crampin, 1997; Shapiro and Kaselow, 2005) in which variations in microstructural parameters are defined as a function of stress and related to the overall elastic properties of the rock via an effective-medium model. In this paper, we consider the generalized effective-medium approach of Schoenberg and Sayers (1995). In this approach, the elasticity of a rock is evaluated in terms of the stiffness of its mineral components and presence of low-volume displacement discontinuities, which serve to increase compliance. This model is highly generalized, and few assumptions need to be made about the discontinuities. By assuming that discontinuities can be considered as rotationally invariant cracks, we can extend the model by using the methods available to describe such discontinuities (e.g., Sayers and Kachanov, 1995; Hudson et al., 1996; Hall, 2000) and how they might vary with pressure (e.g., Tod, 2002).

Following the approach of Tod (2002), we develop a simple model to describe the change in elasticity of a rock as a function of the stress applied to it. This approach is capable of considering anisotropy that develops because of intrinsic rock properties and as a result of nonhydrostatic stresses. It also is capable of providing a framework within which we might consider damage caused by coring or thermal effects. In a subsequent paper, we will integrate this effective nonlinear-elasticity approach with output from coupled geomechanical/fluid-flow simulations to generate elastic models for the prediction of time-lapse seismic properties.

THEORETICAL BACKGROUND

Schoenberg and Sayers (1995) introduce an effective-medium approach to describe the compliance S_{ijkl} of a damaged rock,

$$\varepsilon_{ij} = S_{ijkl}\sigma_{kl} \tag{1}$$

where ε_{ij} is the average strain over a volume caused by an applied stress σ_{kl}. This approach is defined in terms of a matrix material and a random distribution of low-volume, poorly bonded discontinuities. When a stress is applied across such a discontinuity, there will be a difference in displacement between the faces — a displacement discontinuity $[u_i]$ — that is, proportional to the traction, $t_i = \sigma_{ij}n_j$, on the discontinuity surface S. Hence, for a discontinuity with normal $\mathbf{n}$, the total displacement discontinuity $[u_i]$ is given by

$$\int_S [u_i]dS \propto \sigma_{ij}n_j. \tag{2}$$

The total additional strain within a volume V, because of the presence of a set of discontinuities x, is written

$$\varepsilon_{ij} = S^b_{ijkl}\sigma_{kl} + \frac{1}{2V}\sum_x \int_{S_x} \left([u_i]n_j + [u_j]n_i\right)dS, \tag{3}$$

where S^b_{ijkl} is the background compliance of the rock matrix in the absence of discontinuities. This can be estimated by calculating the Voigt average moduli based on individual mineral elasticities and their relative modal proportions (Kendall et al., 2007) using

$$\mathbf{C}^b_V = \sum_{i=1}^{N} f_i\mathbf{C}^m_i, \tag{4}$$

where $\mathbf{C}^b_V$ is the effective or average stiffness, f_i is the volume fraction of mineral constituent i, and $\mathbf{C}^m_i$ is the mineral stiffness. In the absence of mineral-stiffness data, the stiffness $\mathbf{C}^b_V$ can be estimated from the behavior of the rock at high pressures (Sayers, 2002). Equation 3 can be rewritten as

$$\varepsilon_{ij} = \left(S^b_{ijkl} + \Delta S_{ijkl}\right)\sigma_{kl}, \tag{5}$$

where ΔS_{ijkl} is the additional compliance caused by the presence of displacement discontinuities. For a set of displacement discontinuities that are considered as planar features rotationally invariant around $\mathbf{n}$, ΔS_{ijkl} is given by Sayers and Kachanov (1995) as

$$\Delta S_{ijkl} = \frac{1}{4}\left(\delta_{ik}\alpha_{jl} + \delta_{il}\alpha_{jk} + \delta_{jk}\alpha_{il} + \delta_{jl}\alpha_{ik}\right) + \beta_{ijkl}, \tag{6}$$

where δ_{ij} is the Kronecker delta. The second- and fourth-rank tensors α_{ij} and β_{ijkl} are given by

$$\alpha_{ij} = \frac{1}{V}\sum_x B^x_T n^x_i n^x_j S^x$$

$$\beta_{ijkl} = \frac{1}{V}\sum_x \left(B^x_N - B^x_T\right)n^x_i n^x_j n^x_k n^x_l S^x. \tag{7}$$

B^x_N and B^x_T characterize the normal and tangential compliances across an individual discontinuity surface. For a planar, penny-shaped crack with radius r, in a drained, anisotropic rock with Young's modulus E_i and Poisson's ratio ν_i (e.g., Turley and Sines, 1971), B_N and B_T in the direction i normal to the surface are given by Sayers and Kachanov (1995) as

$$B_N = \frac{16\left(1 - \nu_i^2\right)r}{3\pi E_i}, \quad B_T = \frac{32\left(1 - \nu_i^2\right)r}{3\pi E_i\left(2 - \nu_i\right)}. \tag{8}$$

These equations are equivalent to those provided by Hudson (1980) for penny-shaped cracks in the limit that the infilling material has zero bulk modulus.

Sayers (2002) provides a set of equations describing the stiffness tensor of a rock in terms of the 6×6 compliance matrix S^b_{ij} (the 81-component tensor S^b_{ijkl} is condensed using Voigt notation), α_{ij}, and β_{ijkl}. Hall et al. (2007) extend these terms to include the presence of an anisotropic background medium with orthorhombic symmetry,

the principal axes of which are aligned with those of α_{ij}, finding that

$$\begin{aligned}
C_{11} &= \left(\left(S^b_{23} + \beta_{2233}\right)^2 - \left(S^b_{22} + \alpha_{22} + \beta_{2222}\right)\right. \\
&\quad \left.\times\left(S^b_{33} + \alpha_{33} + \beta_{3333}\right)\right)/D, \\
C_{22} &= \left(\left(S^b_{13} + \beta_{1133}\right)^2 - \left(S^b_{11} + \alpha_{11} + \beta_{1111}\right)\right. \\
&\quad \left.\times\left(S^b_{33} + \alpha_{33} + \beta_{3333}\right)\right)/D, \\
C_{33} &= \left(\left(S^b_{12} + \beta_{1122}\right)^2 - \left(S^b_{11} + \alpha_{11} + \beta_{1111}\right)\right. \\
&\quad \left.\times\left(S^b_{22} + \alpha_{22} + \beta_{2222}\right)\right)/D; \qquad (9)
\end{aligned}$$

$$\begin{aligned}
C_{12} &= \left(\left(S^b_{12} + \beta_{1122}\right)\left(S^b_{33} + \alpha_{33} + \beta_{3333}\right)\right. \\
&\quad \left. - \left(S^b_{13} + \beta_{1133}\right)\left(S^b_{23} + \beta_{2233}\right)\right)/D, \\
C_{13} &= \left(\left(S^b_{13} + \beta_{1133}\right)\left(S^b_{22} + \alpha_{22} + \beta_{2222}\right)\right. \\
&\quad \left. - \left(S^b_{12} + \beta_{1122}\right)\left(S^b_{23} + \beta_{2233}\right)\right)/D, \\
C_{23} &= \left(\left(S^b_{23} + \beta_{2233}\right)\left(S^b_{11} + \alpha_{11} + \beta_{1111}\right)\right. \\
&\quad \left. - \left(S^b_{12} + \beta_{1122}\right)\left(S^b_{13} + \beta_{1133}\right)\right)/D; \qquad (10)
\end{aligned}$$

$$\begin{aligned}
C_{44} &= \left(S^b_{44} + \alpha_{22} + \alpha_{33} + 4\beta_{2233}\right)^{-1}, \\
C_{55} &= \left(S^b_{55} + \alpha_{11} + \alpha_{33} + 4\beta_{1133}\right)^{-1}, \\
C_{66} &= \left(S^b_{66} + \alpha_{11} + \alpha_{22} + 4\beta_{1122}\right)^{-1}; \qquad (11)
\end{aligned}$$

$$\begin{aligned}
D &= \left(S^b_{11} + \alpha_{11} + \beta_{1111}\right)\left(S^b_{23} + \beta_{2233}\right)^2 + \left(S^b_{22} + \alpha_{22}\right. \\
&\quad \left. + \beta_{2222}\right)\left(S^b_{13} + \beta_{1133}\right)^2 + \left(S^b_{33} + \alpha_{33} + \beta_{3333}\right)\left(S^b_{12}\right. \\
&\quad \left. + \beta_{1122}\right)^2 - 2\left(S^b_{12} + \beta_{1122}\right)\left(S^b_{13} + \beta_{1133}\right)\left(S^b_{23}\right. \\
&\quad \left. + \beta_{2233}\right) - \left(S^b_{11} + \alpha_{11} + \beta_{1111}\right)\left(S^b_{22} + \alpha_{22}\right. \\
&\quad \left. + \beta_{2222}\right)\left(S^b_{33} + \alpha_{33} + \beta_{3333}\right). \qquad (12)
\end{aligned}$$

Based on work by Gueguen and Schubnel (2003), Hall et al. (2007) introduce an anisotropic normalizing factor h_i, where

$$h_i = \frac{3E_i\left(2 - \nu_i\right)}{32\left(1 - \nu_i^2\right)}. \qquad (13)$$

When α_{ij} is multiplied by this factor, a nondimensional discontinuity-density tensor is returned, which is only a function of discontinuity number density, diameter cubed, and orientation distribution. Summing the diagonal components of α_{ij} normalized by h_i, it is possible to show that

$$\sum_i h_i \alpha_{ii} = \eta_c, \qquad (14)$$

where $\eta_c = Nr^3/V$. N is the number of discontinuities in a volume V, and η_c is equivalent to the nondimensional crack-density term used in many effective-medium theories, such as in Hudson (1980), Hudson et al. (1996), and Thomsen (1995).

Inversion for scalar cracks

From equation 8, we can express the ratio

$$B_N/B_T = \left(1 - \nu_i/2\right). \qquad (15)$$

Sayers and Kachanov (1995)define the scalar crack as $B_N/B_T \approx 1$ to simplify various expressions and make elasticity estimates more treatable. In making this simplification, they assume a rock with low Poisson's ratio ($\nu_o < 0.2$), where β_{ijkl} will be at least an order of magnitude smaller than α_{ij} and can be neglected. In this limit, any crack set can be described by considering its contribution to the three orthogonal components of the second-rank tensor, α_{11}, α_{22}, and α_{33}. For instance, a random isotropic distribution can be described by $\alpha_{11} = \alpha_{22} = \alpha_{33}$ and transverse symmetry by $\alpha_{11} > \alpha_{22} = \alpha_{33}$. Later, we will discuss effects of including β_{ijkl} in the inversion procedure.

Hall et al. (2007) develop an inversion procedure to determine α_{ij} based on observed velocity measurements, assuming $\beta_{ijkl} = 0$. Equations 9–12 are used to relate the observed stiffness tensor, as determined from velocity measurements, to the background stiffness and α_{ij}. An iterative Newton-Raphson approach is used in which a Jacobian matrix describes the variation of the modeled stiffness tensor with α_{ij}. It is assumed that velocity measurements are aligned with principal axes of α_{ij}.

Figure 1 shows results of this inversion procedure for several samples from the Clair reservoir. Cores have been taken from depths of 1784, 1788, 1909, 1950, and 2194 m. Individual samples will be referred to hereafter by their depths. The background compliances were determined using the geomathematical method described by Kendall et al. (2007). X-ray texture goniometry (XRTG) and electron backscattering diffraction (EBSD) were used to assess the preferred orientation of anisotropic minerals or crystal preferred orientation (CPO). Mineral modal proportions were measured using quantitative X-ray diffraction (QXRD). The left panels show the best-fit crack-density α_{ij} values normalized by h_i, and the right panels compare back-calculated velocities with the observed velocities. Back-calculated velocities generally show a reasonable fit with observed velocities, especially for P-waves (V_P). The fit for V_{P45} is poor. Hall et al. (2007) suggest that this might be a result of difficulties in cutting and analyzing the core at 45°.

Joint inversion for α_{ij} and β_{ijkl}

For the scalar crack assumption to be appropriate, rocks must have a low Poisson's ratio, which is acceptable generally for reservoir rocks, and cracks must be flat, poorly bonded features. If there are significant amounts of diagenetic clay or debris within cracks, then equation 15 might not be valid. To model how cracks are influenced by pressure, we make the assumption that they are planar, penny-shaped features without any fill (see next section). By analyzing the contribution of β_{ijkl}, we can discuss how appropriate this assumption is.

Hall et al. (2007) provide a method for estimating β_{ijkl} from velocity measurements, based on Sayers (2002). However, this method assumes that the contribution from β_{ijkl} is small and is responsible solely for the misfit between observed and back-calculated velocities from the inversion for α_{ij}. We wish to test the assumption that β_{ijkl} is small, and so we develop an inversion procedure in which β_{ijkl} is not required a priori to be small.

We assume that cracks are disc shaped, identical, and that β_{ijkl} is isotropic (to do otherwise would introduce impractical complexity

given that our principal aim is to evaluate the magnitude of β_{ijkl} rather than its orientation distribution). We note that for such a distribution, we can rewrite equation 7 for α_{ij} and β_{ijkl} (Sarout et al., 2007)

$$\alpha_{ij} = \frac{\pi N r^2}{3V} B_T \delta_{ij},$$

$$\beta_{ijkl} = \frac{\pi N r^2}{15V}(B_N - B_T)(\delta_{ij}\delta_{kl} + 2(\delta_{ik}\delta_{jl} + \delta_{il}\delta_{jk})). \tag{16}$$

The nonvanishing components of α_{ij} and β_{ijkl} are

$$\alpha_{11} = \alpha_{22} = \alpha_{33} = \frac{1}{3}\alpha_{mm},$$

$$\beta_{1111} = \beta_{2222} = \beta_{3333},$$

$$\beta_{1122} = \beta_{1133} = \beta_{2233} = \beta_{1212} = \beta_{1313} = \beta_{2323} = \frac{1}{3}\beta_{1111}, \tag{17}$$

where

$$\alpha_{11} = \frac{\pi N r^2}{3V} B_T, \tag{18}$$

$$\beta_{1111} = \frac{\pi N r^2}{3V} B_T \left(\frac{B_N}{B_T} - 1\right), \tag{19}$$

and α_{mm} is the trace of α_{ij}($\alpha_{mm} = \alpha_{11} + \alpha_{22} + \alpha_{33}$). By rearranging equations 18 and 19, we can rewrite β_{ijkl} in terms of α_{ij} and the ratio B_N/B_T, such that

$$\beta_{1111} = \frac{1}{3}\left(\frac{B_N}{B_T} - 1\right)\alpha_{mm}. \tag{20}$$

Substituting this relationship, we can rewrite equations 9–12 solely in terms of α_{ij} and the ratio B_N/B_T.

We then use an inversion approach similar to that discussed for the scalar cracks above, but we include a grid search over B_N/B_T to find the value that minimizes the misfit between observed and back-calculated velocities at each measured pressure. The results of this inversion for the Clair samples are shown in Figure 2. Figure 3a shows optimum values of B_N/B_T determined via this method.

We also perform the inversion for Berea (Lo et al., 1986) and Penrith (Sayers, 2002) sandstone samples. Because EBSD and XRTG information is not available for these samples, S^b_{ij} is determined from the behavior of samples at high pressure after MacBeth (2004). Results are shown in Figure 4, with B_N/B_T plotted in Figure 3b. At high pressures, observed stiffness tensors become close to S^b_{ij}; hence, α_{ij} becomes small, and our inversion for B_N/B_T becomes less reliable. This problem is not encountered by Clair samples in which the observed stiffness is always well below S^b_{ij}.

Figure 3 gives an indication as to how appropriate the scalar crack assumption is. For a flat crack with no infill, equation 15 suggests that B_N/B_T should be between 0.8 and 1, depending on the Poisson's ratio of the background matrix. Although there is some spread outside these bounds, the majority of inverted B_N/B_T values are found close to this range, indicating that the scalar crack assumption is appropriate. It also is worth noting that there appears to be no systematic variation of B_N/B_T with pressure, which is predicted implicitly by the scalar crack assumption, further strengthening our confidence in making it.

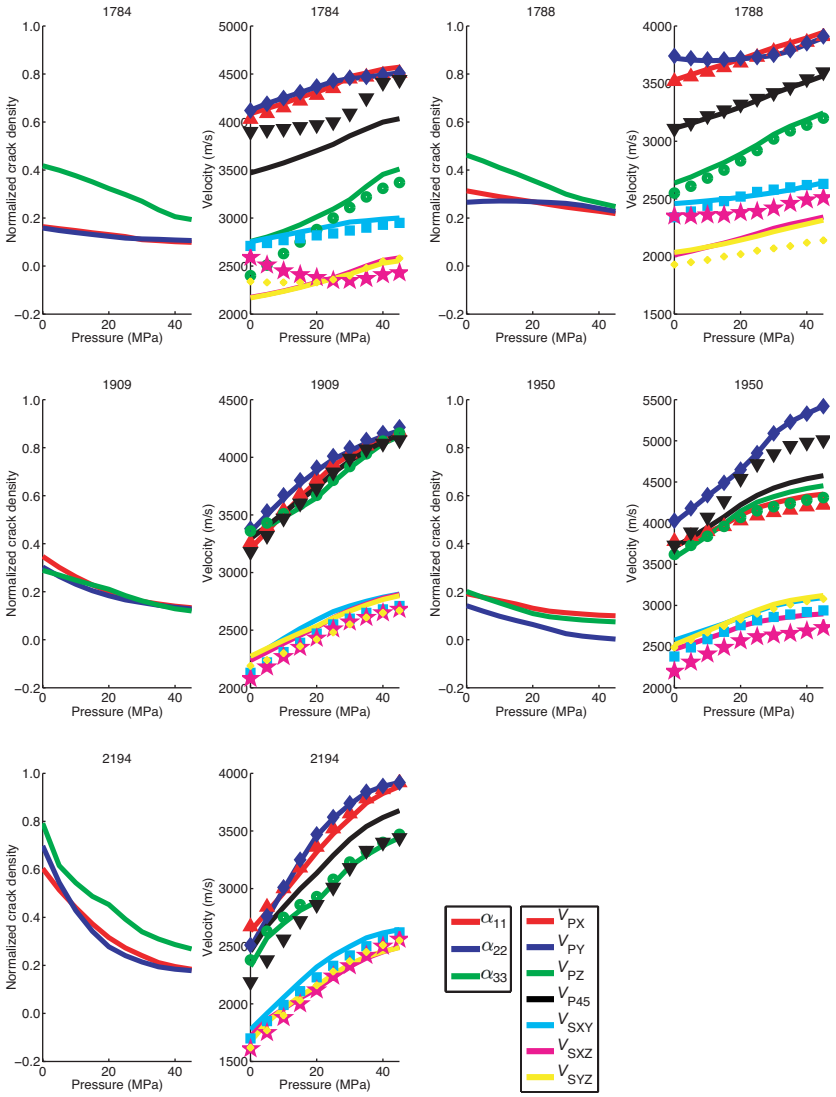

Figure 1. Inverted scalar crack densities and back-calculated velocities for Clair samples. Left-hand panels show α_{ij} as a function of pressure. Right-hand panels show observed velocity data (symbols) and back-calculated velocities (lines) corresponding to calculated α_{ij} values.

EFFECTS OF STRESS ON CRACK DENSITY

We know from microstructural analysis (e.g., Batzle et al., 1980) that cracks and discontinuities are complex features, with rough walls, nonlinear geometry, irregular intersections, and clay or diagenetic infill. However, in the previous section, we have shown that by modeling them as highly simplified, rotationally invariant, smooth (penny-shaped), empty features, we still can approximate the effective rock properties to a reasonable degree of accuracy. We use this observation to our advantage to predict how the effective properties will be influenced by an applied stress field.

Hudson (2000) and Tod (2002) present analytical models in which the aspect ratio and number density of cracks are dependent on applied stress and fluid pressure. This model considers only elastic deformation in which permanent deformation of pores into cracks and development of new cracks are not considered. Hence, when the stress state is returned to its original magnitude, the material will relax to its reference state. In other words, this assumption will be appropriate only as long as the rock does not undergo any plastic or brittle deformation. However, this assumption might be sufficient for application to 4D seismic modeling.

Hudson (2000) derives an expression for the change in aspect ratio δa of a penny-shaped crack caused by a change in applied stress and/or fluid pressure,

$$\delta a = -\frac{2(1-\nu_b)}{\pi\mu_b}\left(\delta\sigma_{ij}n_in_j - \beta_w\delta P_{fl}\right) - \frac{a}{K_b}\beta_w\delta P_{fl}, \quad (21)$$

where $\delta\sigma_{ij}$ and δP_{fl} are the change in applied stress tensor and fluid pressure; β_w is the Biot-Willis parameter, assumed here for simplicity to be unity; $\mathbf{n}$ is the crack normal; and μ_b and K_b are the shear and bulk moduli of the matrix in the absence of compliant porosity, respectively. The right-hand term $a\beta_w\delta P_{fl}/K_b$ of equation 21 is small compared with other terms and can be neglected (Hudson, 2000). Integrating equation 21 gives

$$a = a^0 - \frac{2(1-\nu)_b}{\pi\mu_b}\sigma^{c(\mathbf{n})}, \quad (22)$$

where a^0 is the aspect ratio in the absence of an applied stress (or at a predefined reference stress). The effects of applied stress and pore pressure combine to give the effective crack normal stress

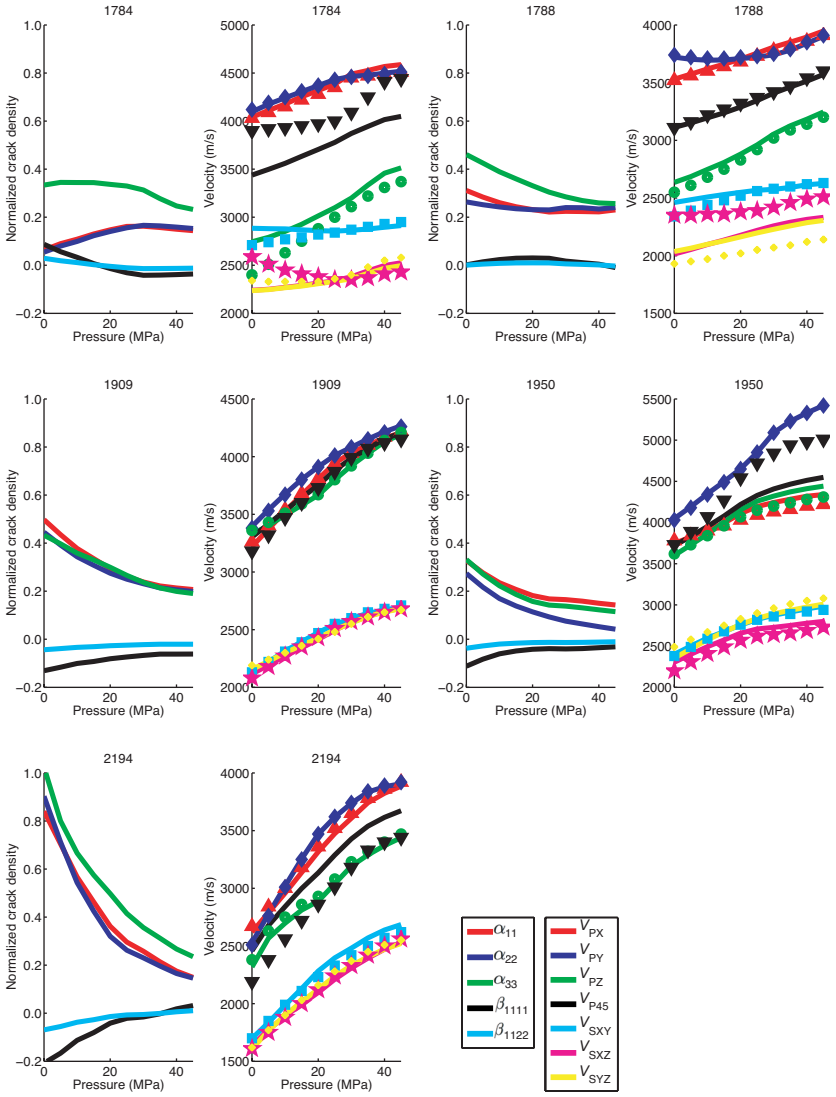

Figure 2. Inverted second- and fourth-rank crack-density tensor components and back-calculated velocities for Clair samples. Left-hand panels show α_{ij} and β_{ijkl} as a function of pressure. Right-hand panels show observed velocity data (symbols) and back-calculated velocities (lines) corresponding to calculated α_{ij} and β_{ijkl} values.

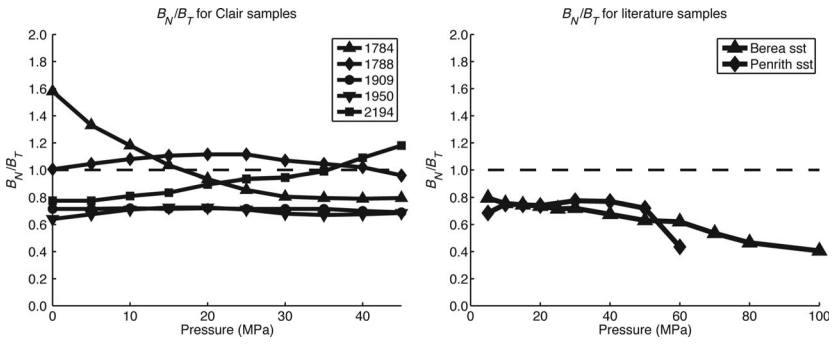

Figure 3. Best-fit B_N/B_T as a function of pressure for (a) Clair samples and (b) literature samples.

$$\sigma^{c(\mathbf{n})} = \sigma_{ij} n_i n_j - \beta_w P_{fl}. \quad (23)$$

For a crack with an initial aspect ratio a^0, there will be a critical stress where

$$a^0 = \frac{2(1-\nu)_b}{\pi \mu_b} \sigma^{c(\mathbf{n})}, \quad (24)$$

and the crack can be considered as closed. Tod (2002) assumes an exponential distribution of initial aspect ratios. If this is the case, crack density will decrease exponentially as cracks close under pressure (van der Neut et al., 2007), so that

$$\xi(\sigma^c) = \xi^0 \exp(-c_r \sigma^{c(\mathbf{n})}), \quad (25)$$

where

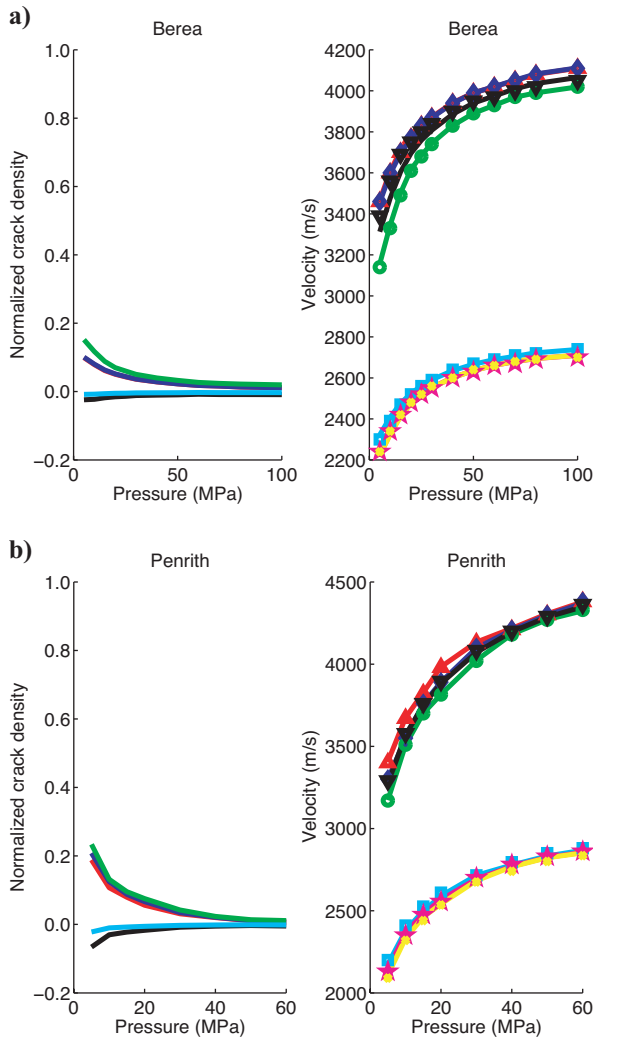

Figure 4. Inverted second- and fourth-rank crack-density tensor components and back-calculated velocities for the literature samples: (a) Berea Sandstone, (b) Penrith Sandstone. Left-hand panels show α_{ij} and β_{ijkl} as a function of pressure. Right-hand panels show observed velocity data (symbols) and back-calculated velocities (lines) corresponding to calculated α_{ij} and β_{ijkl} values. The legend for this figure is the same as for Figure 2.

$$c_r = \frac{2(1-\nu_b)}{\pi \mu_b a^0} \quad (26)$$

and ξ^0 is the crack density at a defined initial pressure (usually 0 MPa).

As discussed in the previous section, by making the scalar crack assumption, we treat the overall crack distribution as three mutually orthogonal aligned sets, each contributing to one of the nonzero components of α_{ij}. For each set, an initial crack density and average aspect ratio are defined. Hence, for any applied stress field, α_{ij} is calculated using equations 25 and 26 to give

$$\alpha_{ij} = \begin{pmatrix} \xi_1(\sigma^{c(\mathbf{n}_1)})/h_1 & 0 & 0 \\ 0 & \xi_2(\sigma^{c(\mathbf{n}_2)})/h_2 & 0 \\ 0 & 0 & \xi_3(\sigma^{c(\mathbf{n}_3)})/h_3 \end{pmatrix}. \quad (27)$$

Results

Figure 5 shows results of modeling the P- and S-wave velocities using equations 25–27 for samples discussed in the previous section. Table 1 shows the best-fit initial average aspect ratios and crack densities used to produce these models.

The fit between observed and modeled velocities is reasonable. Furthermore, initial aspect ratios range between $5 \times 10^{-4} < a^0 < 5 \times 10^{-3}$, which is a reasonable range of values expected for a distribution of flat, penny-shaped cracks (Kuster and Toksöz, 1974). Results from Figure 5 and Table 1 indicate that the nonlinear elastic behavior can be modeled based on the assumption that it is made of stiff, nondeforming mineral grains and displacement discontinuities in the form of flat, penny-shaped cracks with physically reasonable initial aspect ratio distributions.

DISCUSSION

Anisotropy

A benefit of our approach is the treatment of anisotropy. This model is capable of considering intrinsic anisotropy as well as stress induced anisotropy. Most rocks are intrinsically anisotropic. This intrinsic anisotropy is derived from two sources: alignment of minerals and alignment of fabrics.

Alignment of mineral grains caused by depositional, deformation, or diagenetic processes (CPO) has been well studied as a cause of anisotropy. Elongate or platy minerals, such as micas and clays, will tend to become aligned during deposition. Elasticities of these minerals can be highly anisotropic, with the principal axes of the elastic tensor aligned with grain shape. By using the geomathematical model developed by Kendall et al. (2007) to evaluate the background compliance S^b_{ijkl}, we can assess the contribution of CPO to the anisotropy of a sample based on detailed petrofabric analysis. Equations 9–12 limit us to cases in which the principal axes of the compliance tensor and α_{ij} are aligned. This should not pose a problem for vertical transverse isotropy (VTI) systems as long as one of the principal stress axes is aligned vertically. However, more complicated anisotropic symmetries will need to be dealt with carefully.

Shape-preferred orientation (SPO) anisotropy also is related to alignment of fabric during sedimentary deposition and/or diagenesis. If platy or elongate grains are deposited so that there is a preferential alignment between grain contacts, there will be an increase in

displacement discontinuities in this direction and hence an increased compliance. This effect is demonstrated best by Clair samples 1784 and 1788 (Hall et al., 2007). These samples are rich in mica, and platy grains are orientated with normals parallel to the z-axis. In this case, we expect to find a greater number of grain boundaries with normals parallel to the z-axis than to the x- or y-axis. As a result, V_{Pz} is reduced greatly (Figure 1), and our inversion for α_{ij} indicates that α_{33} is larger than α_{11} and α_{22}. Because the preferred orientation of mineralogic axes and grain boundaries will not be affected greatly by in situ reservoir stresses (unless these are of sufficient magnitude to cause deformation or failure of mineral grains), we refer to the anisotropy they cause as static anisotropy.

Effects of nonhydrostatic stresses on anisotropy also are expected to be important. For example, effects of uniaxial stresses on seismic anisotropy have been documented (e.g., Scott and Abousleiman, 2004; Sayers and Schutjens, 2007). When the applied stress is uniaxial, cracks with faces perpendicular to the principal stress axis will close, although those parallel will open or remain unaffected. As a result, velocities will be faster in the direction parallel to maximum stress. Because the stress field within and around reservoirs is likely to be nonhydrostatic, it is important that any model used to estimate seismic velocities is capable of incorporating these effects. For example, Herwanger and Horne (2005) model seismic anisotropy caused by a triaxial stress field based on third-order elasticity theory (Prioul et al., 2004) to explain shear-wave splitting observations from the Valhall and Ekofisk fields.

Here we consider nonhydrostatic stresses by resolving the in situ stress field in terms of stresses normal to modeled crack faces. This is shown in Figure 6. Figure 6a shows results of a hydrostatic compression test on a sample of Berea Sandstone (Scott and Abousleiman, 2004), and best-fit ξ^0 and a^0 values used to back-calculate velocities. Scott and Abousleiman (2004) then perform a uniaxial strain test on a similar core sample. Details of the uniaxial test are shown in Figure 6b and c, with results plotted in Figure 6d. The ξ_0 and a^0 values cal-

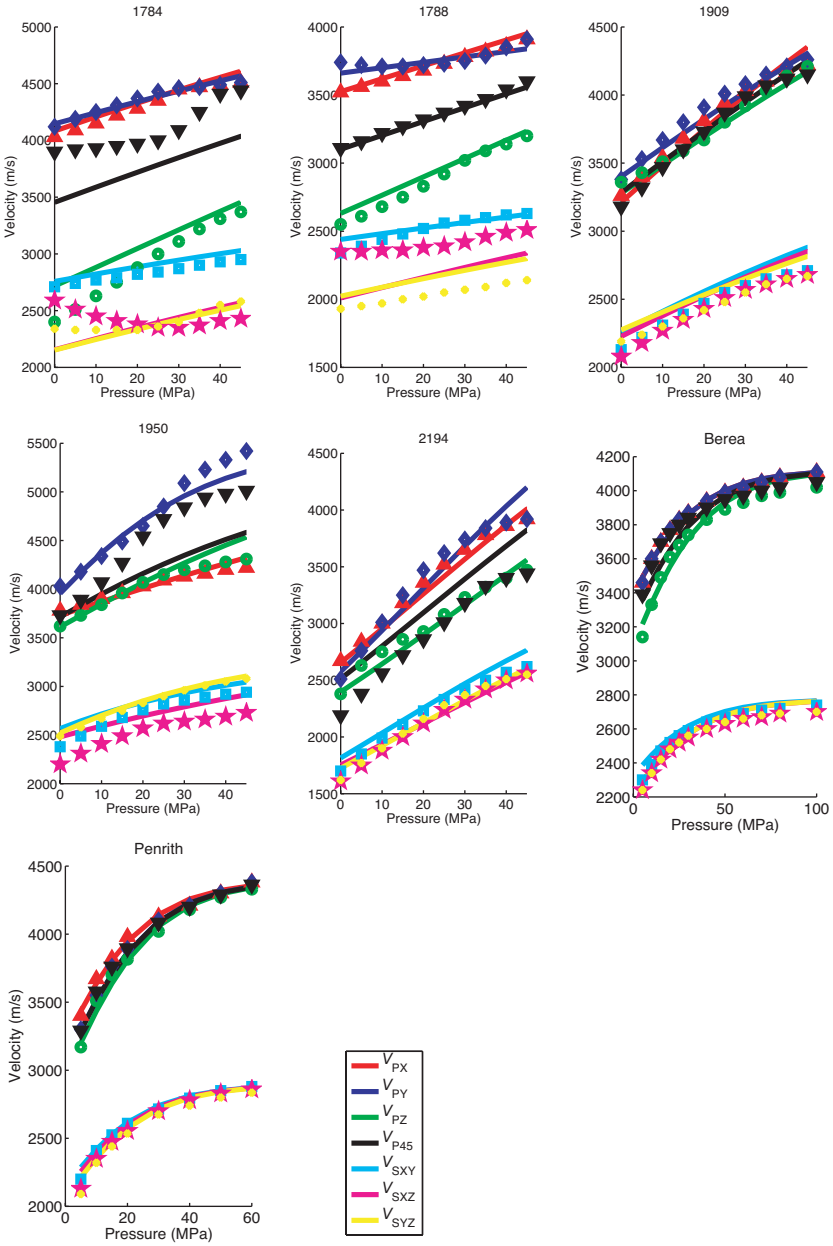

Figure 5. Velocities calculated as a function of hydrostatic stress calculated using equations 25–27 (lines), shown with observed velocity values (symbols).

culated for the hydrostatic case (given in Table 2) then are used to predict velocities for the uniaxial case. It can be seen that with application of this uniaxial stress, the velocity of P-waves along the main axis increases rapidly with pressure, whereas those perpendicular to the main axis increase more slowly. These effects are predicted by our model, and the fit is particularly good for faster P-waves (V_{Px}) and fast S-waves (V_{Syz}) as well as for P-waves at 45°.

The model does not accurately predict the slower P- (V_{Pz}) and S-wave (V_{Sxz}) velocities above a confining pressure of 20 MPa. The model predicts that as confining pressure increases, crack sets oriented parallel to the main axis will close gradually and lead to increasing velocity of slower waves. What is observed is that the anisotropy becomes locked in (Scott and Abousleiman, 2004) and velocities do not increase further. The reason for the locking-in mechanism remains unclear, and thus any improvements to our analytical model will require understanding of this mechanism. It is possible that this failure arises partly because of our assumption that all deformation occurring is elastic. Scott and Abousleiman (2004) observe significant amounts of acoustic emissions at higher stresses for a triaxial stress test, indicating that inelastic deformation indeed is occurring. It also might be possible that crack-crack interactions are affecting deformation in the manner similar to that described by Batzle et al. (1980).

Time-lapse seismic data can show an asymmetry in the P-wave velocity/effective-stress relationship (V_P/σ_{eff}) between stress-up (compaction or pore-pressure depletion) and stress-down (extension or pore-pressure increase) effects (e.g., Hatchell and Bourne, 2005). Observations indicate that the increase in V_P caused by an increase in σ_{eff} is smaller than the decrease caused by an equivalent σ_{eff} decrease. The nonlinear nature of our stress-velocity model means these effects are accounted for to an extent. However, it could be argued that modeled asymmetry between stress-up and stress-down effects is not as large as those observed by Hatchell and Bourne (2005), particularly at higher stresses, in which the rate of change of the velocity/stress gradient ($d^2V_P/d\sigma_{eff}^2$) is lowest (Sayers, 2007). If a degree of irreversible deformation, such as cement breakage, occurs when the rock is moved from its initial stress state, then this will increase the asymmetry, because the decrease in compliance caused by a stress increase will be canceled by the additional compliance induced by inelastic deformation. In the following section, we consider (in a qualitative sense only) how we might deal with inelastic damage within the framework outlined in this paper.

Table 1. Best-fit initial average crack-aspect ratios (a^0) and densities (ξ^0) for the Clair and literature samples used to calculate velocities as a function of stress shown in Figure 5.

Sample	Crack set	a^0	ξ^0	Sample	Crack set	a^0	ξ^0
	α_{11}	0.0014	0.165		α_{11}	0.0006	0.590
1784	α_{22}	0.0018	0.155	2194	α_{22}	0.0005	0.635
	α_{33}	0.0012	0.440		α_{33}	0.0007	0.740
	α_{11}	0.0019	0.315		α_{11}	0.0009	0.085
1788	α_{22}	0.0044	0.280	Berea	α_{22}	0.0009	0.085
	α_{33}	0.0014	0.475		α_{33}	0.0009	0.140
	α_{11}	0.0007	0.345		α_{11}	0.0005	0.150
1909	α_{22}	0.0008	0.295	Penrith	α_{22}	0.0005	0.180
	α_{33}	0.0009	0.300		α_{33}	0.0005	0.210
	α_{11}	0.0014	0.190				
1950	α_{22}	0.0004	0.150				
	α_{33}	0.0008	0.195				

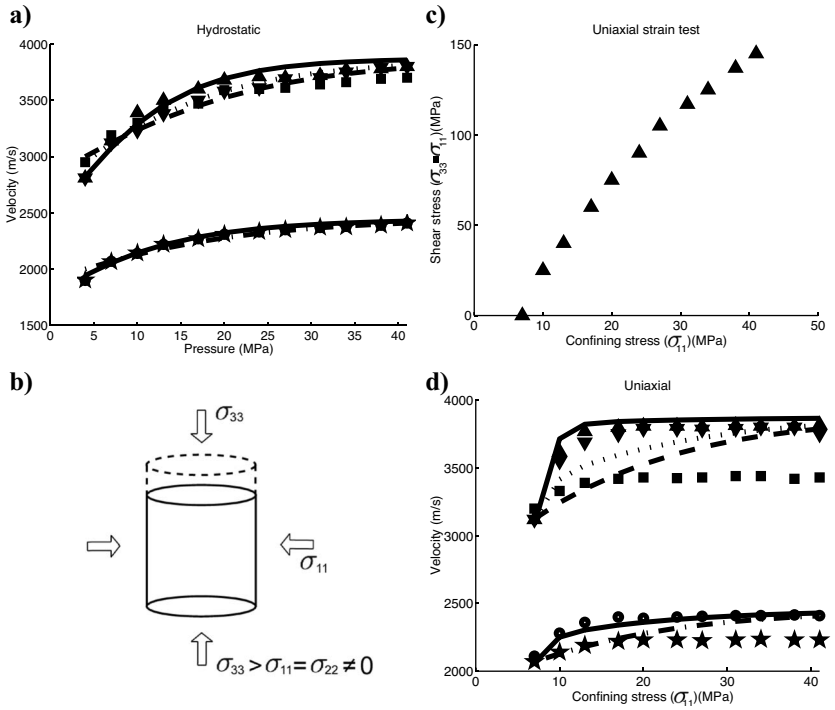

Figure 6. (a) Observed and back-calculated P- and S-wave velocities for hydrostatic compression of Berea Sandstone. (b) and (c) Details of the uniaxial experiment. (d) The best-fit parameters (ξ_0) and a_0) for the hydrostatic case are used to model the uniaxial case. Experimental data (symbols) are from Scott and Abousleiman (2004) (△ — V_{Pz}, □ — V_{Px}, ▽ — V_{P45}, ⋆ — V_{Sxy}, ∘ — V_{Syz}).

Coring and damage

It is becoming increasingly clear among rock physicists that using velocities measured on cored samples might not be representative of velocities of in situ reservoir rocks. Tests comparing synthetic sandstones (e.g., Holt et al., 2000) and comparison of cored samples with well-log mea-

surements (e.g., Furre et al., 2007) indicate that in situ rocks generally have higher velocities and lower stress sensitivity. The explanation forwarded for this is that coring of the sample causes large deviatoric stresses that create permanent damage in the sample. Although this effect is compensated for to some extent because cores generally sample more competent zones of a reservoir and they might miss larger-scale fractures that could increase stress sensitivity, it is of interest to consider how to account for damage caused by coring or other mechanisms within the framework of our model.

MacBeth and Schuett (2007) demonstrate the effect that damage can have on a sample; however, in this case, the damage is caused not by coring but by thermal expansion of grains during heating. Figure 7 shows measurements of ultrasonic P- and S-wave velocities from Rotliegend Sandstone samples before and after they have been damaged by heating. Assuming the isotropic background compliance given by MacBeth and Schuett (2007) and an isotropic α_{ij}, we use equations 25 and 26 to find the optimum values of ξ^0 and a^0 that minimize misfit between observed and modeled velocities.

Table 3 shows the values of ξ^0 and a^0 used to calculate the modeled velocities in Figure 7. It is clear that differences between damaged and undamaged samples can be accounted for solely by the increase in the initial crack density. Thus, the potential exists to remove effects of coring damage from our estimates of stress-dependent elasticity for in situ rocks. At present, however, we cannot estimate how much damage the coring process will cause. Hence, we cannot estimate how much we should decrease our estimates for ξ^0 when upscaling from laboratory measurements to in situ rocks.

The treatment of SPO anisotropy and core damage serves as an indication of how we might interpret the physical meaning of crack density and aspect ratio. We note at this point that these terms have been developed as theoretical parameters to model stress-dependent elasticity. However, they do appear to have a correlation, if only in a qualitative sense, with physical observations such as alignment of elongate or platy grains or the degree of damage done to a sample. This correlation strengthens our confidence in the conceptual validity of the microstructural approach for modeling nonlinear stress-dependent velocities. It is an interesting and as yet unanswered question whether petrofabric analysis techniques can develop quantitative estimates of microstructural parameters independently from velocity observations.

Workflow

Figure 8 outlines the workflow we follow to generate elastic stiffness from geomechanical simulation. Coupled fluid-flow/geomechanical simulation generates information on the in situ stress tensor, pore-fluid pressure, porosity, and fluid properties for each grid cell mapping the overburden and reservoir (Figure 8a). Ultrasonic and petrofabric analysis of core samples allows us to evaluate the background compliance (S^b_{ijkl}) and initial crack parameters (ξ^0 and a^0) for representative lithologies (Figure 8b). After the grid has been populated with these parameters, drained elasticities can be computed using the approach outlined in this paper (Figure 8c). To include effects of fluids on the elasticity of an anisotropic porous medium, the generalized anisotropic Gassmann solution of Brown and Korringa (1975) is used, in which we assume the majority of the pore space consists of equant (spherical) pores and microcracks do not contribute significantly to the poroelasticity. This solution is valid in the low-frequency limit in which squirt flow (e.g., Chapman, 2003) does not occur, so it is assumed to be a suitable approximation for low-frequency seismic energy (Figure 8d). When elasticity has been computed for each grid cell, the full 3D anisotropic elastic model can be used with ray tracing or waveform solvers to predict effects of geomechanical deformation on seismic observables (Figure 8e).

Table 2. Best-fit initial average crack-aspect ratios (a^0) and densities ($\grave{o}^0$) calculated from hydrostatic stress test shown in Figure 6a and used to calculate velocities for the uniaxial stress experiment shown in Figure 6d.

	a^0	ξ^0
α_{11}	0.00031	0.250
α_{22}	0.00061	0.135
α_{33}	0.00061	0.140

Table 3. Best-fit initial average crack-aspect ratios (a_0) and densities (ξ^0) used to generate predicted velocities in Figure 7. Damaged samples show similar initial aspect ratios but much larger initial crack densities.

Sample	a_0	ξ^0
6 H undamaged	0.005	0.07
6 H damaged	0.005	0.27
10 V undamaged	0.005	0.065
10 V damaged	0.005	0.3

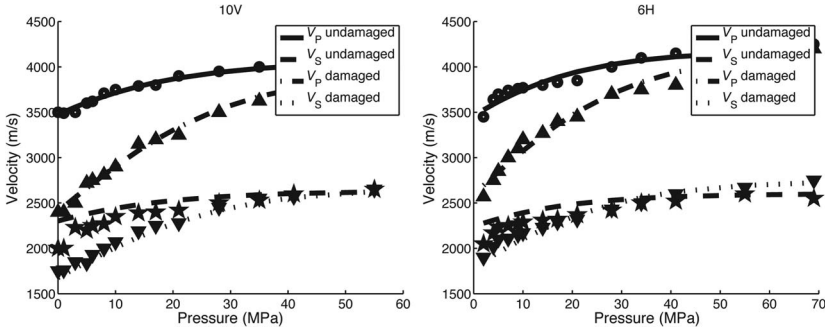

Figure 7. Ultrasonic P- and S-wave velocities measured before and after sandstone samples 6 H and 10 V (from MacBeth and Schuett, 2007) have been damaged by heating. Damaged samples show a much larger stress sensitivity at low pressures. Best-fit initial aspect ratio and crack densities (Table 3) are chosen to model the observed variation of velocity with stress.

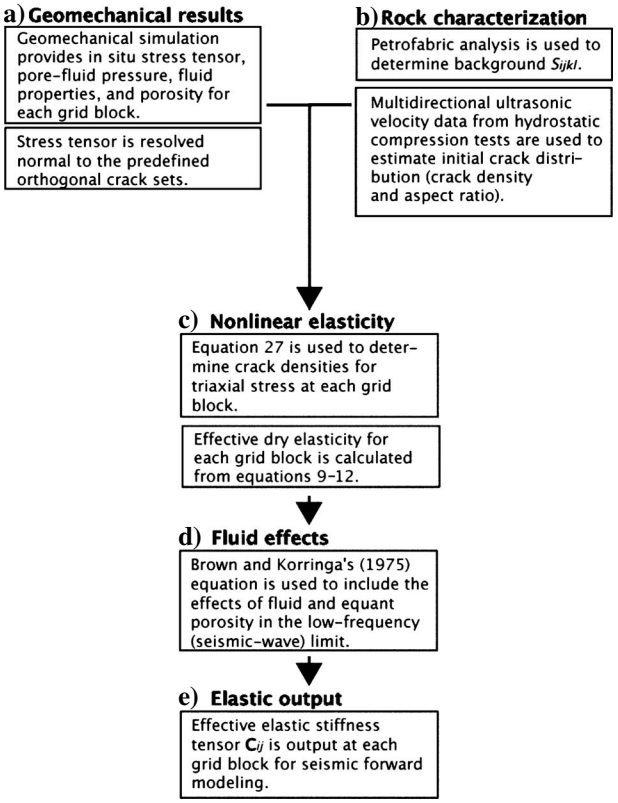

Figure 8. Summary of the workflow used to predict elasticity based on coupled fluid-flow/geomechanical simulation.

CONCLUSIONS

To relate geomechanical modeling to seismic observables, a rock-physics model is required that can relate changes in effective stress applied to a rock with changes in rock stiffness. Such a model should be capable of empirically describing observed stress-velocity effects such as nonlinearity and stress-induced anisotropy. A model that is simple to use and easy to parameterize also is preferable.

We develop a microstructural rock-physics model in which the overall compliance is considered as a function of the compliance of minerals and stiff spherical pores and the additional compliance caused by the presence of low-volume, low-aspect ratio planar discontinuities. Inversions including the fourth-rank crack-density tensor are performed to test the suitability of the scalar crack approximation. Using this approximation, we model the stress-dependent elasticity by considering the displacement discontinuities as three mutually orthogonal sets of low-aspect-ratio, penny-shaped cracks.

Our model has been calibrated experimentally using a set of sandstone samples from a UKCS reservoir and data sets from the literature. We demonstrate that velocity variations between (and within anisotropic) samples are caused by differences in the initial number density of compliant discontinuities. As such, our model is relatively easy to parameterize and yet is capable of considering the effects of anisotropy both, intrinsically within the rock framework and caused by nonhydrostatic stresses.

Our model presumes that microcracks deform elastically. At high stresses, in which inelastic deformation occurs, this might not be appropriate. By considering how damage affects the initial microcrack distribution, we might extend our model to include inelastic deformation. Although this serves to highlight the physical intuitiveness of our model, it remains at present a qualitative approach only. Finally, a workflow is outlined, which illustrates the approach we will use in a subsequent paper to integrate rock physics with output from coupled geomechanical/fluid-flow simulations, to generate elastic models for the prediction of time-lapse seismic properties.

ACKNOWLEDGMENTS

This work was done as part of the IPEGG project, which is sponsored by BP, BG, ENI, and Statoil. James Verdon was supported by a UKERC Interdisciplinary Studentship Award. The authors thank the SAIL project collaborators for the use of Clair reservoir core data. The authors also thank all reviewers, whose comments substantially improved the quality of this paper.

REFERENCES

Batzle, M. L., G. Simmon, and R. W. Siegfried, 1980, Microcrack closure in rocks under stress: Direct observation: Journal of Geophysical Research, **85**, 7072–7090.
Brown, R. J. S., and J. Korringa, 1975, On the dependence of the elastic properties of a porous rock on the compressibility of the pore fluid: Geophysics, **40**, 608–616.
Chapman, M., 2003, Frequency-dependent anisotropy due to meso-scale fractures in the presence of equant porosity: Geophysical Prospecting, **51**, 369–379.
Dean, R., X. Gai, C. Stone, and S. Minkoff, 2003, A comparison of techniques for coupling porous flow and geomechanics: SPE 17th Annual Reservoir Simulation Symposium, SPE 79709.
Furre, A. K., M. Andersen, A. S. Moen, and R. K. Tonnessen, 2007, Sonic log derived pressure depletion predictions and application to time-lapse seismic interpretation: 69th Annual Conference and Exhibition, EAGE, Extended Abstracts, PO77.
Gassmann, F., 1951, Uber die elastizitat poroser medien: Vierteljahresschrift der Naturforschenden Gesellschaft, **96**, 1–23.
Gueguen, Y., and A. Schubnel, 2003, Elastic wave velocities and permeability of cracked rocks: Tectonophysics, **370**, 163–176.
Guilbot, J., and B. Smith, 2002, 4-D constrained depth conversion for reservoir compaction estimation: Application to Ekofisk Field: The Leading Edge, **21**, 302–308.
Hall, S. A., 2000, Rock fracture characterisation and seismic anisotropy: Application to ocean bottom seismic data: Ph.D. thesis, University of Leeds.
Hall, S. A., J. M. Kendall, Q. Fisher, and J. Maddock, 2007, Crack density tensor inversion for analysis of changes in rock frame architecture: 69th Annual Conference and Exhibition, EAGE, Extended Abstracts, FO29.
Hatchell, P., and S. Bourne, 2005, Rocks under strain: Strain-induced time-lapse time shifts are observed for depleting reservoirs: The Leading Edge, **24**, 1222–1225.
Herwanger, J., and S. Horne, 2005, Predicting time-lapse stress effects in seismic data: The Leading Edge, **24**, 1234–1242.
Holt, R. M., M. Brignoli, and C. J. Kenter, 2000, Core quality: Quantification of coring-induced rock alteration: International Journal of Rock Mechanics and Mining Science, **37**, 889–907.
Hudson, J. A., 1980, Overall properties of a cracked solid: Mathematical Proceedings of the Cambridge Philosophical Society, **88**, 371–384.
——, 2000, The effect of fluid pressure on wave speeds in a cracked solid: Geophysical Journal International, **143**, 302–310.
Hudson, J. A., E. Liu, and S. Crampin, 1996, The mechanical properties of materials with interconnected cracks and pores: Geophysical Journal International, **124**, 105–112.
Kendall, J. M., Q. J. Fisher, S. C. Crump, J. Maddock, A. Carter, S. A. Hall, J. Wookey, S. Valcke, M. Casey, G. Lloyd, and W. B. Ismail, 2007, Seismic anisotropy as an indicator of reservoir quality of siliclastic rocks, *in* S. Jolley, D. Barr, J. Walsh, and R. J. Knipe, eds., Structurally complex reservoirs: Geological Society Special Publication 292, 123–136.
Kuster, G. T., and M. N. Toksöz, 1974, Velocity and attenuation of seismic waves in two-phase media: Part I: Theoretical formulations: Geophysics, **39**, 587–606.
Lo, T. W., K. B. Coyner, and M. N. Toksöz, 1986, Experimental determination of elastic anisotropy of Berea Sandstone, Chicopee Shale, and Chelmsford Granite: Geophysics, **51**, 164–171.
MacBeth, C., 2004, A classification for the pressure-sensitivity properties of a sandstone rock frame: Geophysics, **69**, 497–510.
MacBeth, C., and H. Schuett, 2007, The stress dependent elastic properties of

thermally induced microfractures in aeolian Rotliegend Sandstone: Geophysical Prospecting, **55**, 323–332.
Makse, H. A., N. Gland, D. L. Johnson, and L. M. Schwartz, 1999, Why effective medium theory fails in granular materials: Physical Review Letters, **83**, 5070–5073.
McLellan, P., 1996, Assessing the risk of wellbore instability in horizontal and inclined wells: Journal of Canadian Petroleum Technology, **35**, 21–32.
Minkoff, S. E., C. M. Stone, S. Bryant, and M. Peszynska, 2004, Coupled geomechanics and flow simulation for time-lapse seismic modeling: Geophysics, **61**, 200–211.
Nur, A., and G. Simmons, 1969, The effect of saturation on velocity in low porosity rocks: Earth and Planetary Science Letters, **7**, 183–193.
Prioul, R., A. Bakulin, and V. Bakulin, 2004, Nonlinear rock physics model for estimation of 3D subsurface stress in anisotropic formations: Theory and laboratory verification: Geophysics, **69**, 415–425.
Sarout, J., L. Molez, Y. Gueguen, and N. Hoteit, 2007, Shale dynamic properties and anisotropy under triaxial loading: Experimental and theoretical investigations: Physics and Chemistry of the Earth, **32**, 896–906.
Sayers, C. M., 2002, Stress-dependent elastic anisotropy of sandstones: Geophysical Prospecting, **50**, 85–95.
——–, 2007, Asymmetry in the time-lapse seismic response to injection and depletion: Geophysical Prospecting, **55**, 1–7.
Sayers, C. M., and M. Kachanov, 1995, Microcrack induced elastic wave anisotropy of brittle rocks: Journal of Geophysical Research, **100**, 4149–4156.
Sayers, C. M., and P. T. Schutjens, 2007, An introduction to reservoir geomechanics: The Leading Edge, **26**, 597–601.
Schoenberg, M., and C. M. Sayers, 1995, Seismic anisotropy of fractured rock: Geophysics, **60**, 204–211.
Scott, T. E., and Y. Abousleiman, 2004, Acoustical imaging and mechanical properties of soft rock and marine sediments: Technical Report 15302, U. S. Department of Energy, accessed April 1, 2004; http://www.osti.gov/energycitations/purl.cover.jsp?purl=/828441-uiLUfO/native/.
Shapiro, S. A., and A. Kaselow, 2005, Porosity and elastic anisotropy of rocks under tectonic stress and pore-pressure changes: Geophysics, **70**, no. 5, N27–N38.
Thomsen, L., 1995, Elastic anisotropy due to aligned cracks in porous rock: Geophysical Prospecting, **43**, 805–829.
Tod, S. R., 2002, The effects of stress and fluid pressure on the anisotropy of interconnected cracks: Geophysical Journal International, **149**, 149–156.
Turley, J., and G. Sines, 1971, The anisotropy of Young's modulus, shear modulus and Poisson's ratio in cubic materials: Journal of Physics D: Applied Physics, **4**, 264–271.
van der Neut, J. R., M. K. Sen, and K. Wapenaar, 2007, Monitoring effective stress changes in fault zones from time-lapse seismic reflection data — A model study: 69th Annual Conference and Exhibition, EAGE, Extended Abstracts, PO61.
Zatsepin, S., and S. Crampin, 1997, Modelling the compliance of crustal rock — I. Response of shear-wave splitting to differential stress: Geophysical Journal International, **129**, 477–494.